Supplementary Information Available

The mechanism of aquaporin inhibition by gold compounds elucidated by biophysical and computational methods

Andreia de Almeida,[a,†] Andreia F. Mósca,[b,c,†] Darren Wragg, [a] Margot Wenzel, [a] Paul Kavanagh,[d]

Giampaolo Barone,[e] Stefano Leoni, [a] Graça Soveral, [b,c] * Angela Casini[1]*

[a] *School of Chemistry, Cardiff University, Main Building, Park Place, Cardiff CF10 3AT, United Kingdom.*

[b] *Research Institute for Medicines (iMed.ULisboa), Faculty of Pharmacy, Universidade de Lisboa, 1649-003 Lisboa, Portugal.*

[c] *Dept. Bioquímica e Biologia Humana, Faculty of Pharmacy, Universidade de Lisboa, 1649-003 Lisboa, Portugal*

[d] *School of Chemistry and Chemical Engineering, Queen's University Belfast, David Keir Building, Stranmillis Road, Belfast, BT9 5AG, United Kingdom.*

[e] *Dip. di Scienze e Tecnologie Biologiche, Chimiche e Farmaceutiche (STEBICEF), Università degli Studi di Palermo, Viale delle Scienze Ed. 17, 90128, Palermo, Italy.*

Experimental Section

Materials and Methods: Gold compounds **1-3** were prepared according to literature procedures.[1-4] The purity of the compounds was confirmed by elemental analysis, and all of them showed purity greater than 98%. 1,10-phenantroline and 2-mercaptoethanol were from Sigma. ^1H NMR spectra were recorded on a Bruker Avance II400 spectrometer at room temperature (r.t.). Elemental analyses were performed on a Carlo Erba EA 1110 CHN instrument. ESI-MS spectra were obtained in acetonitrile on a Thermo Finnigan LCQ DecaXPPlus quadrupole ion-trap instrument operated in positive ion mode over a mass range of m/z 150–2000. The absorption spectra of the complexes **3** and **4** in the UV-Visible region were recorded on a Cary 5000 UV-Visible NIR spectrophotometer.

Synthesis of Au(2-(pyridin-2-yl)-1H-benzo[d]imidazole)Cl$_2$ – 3: To a solution of (2-(pyridin-2-yl)-benzimidazole) (0.195 g, 1.00 mmol) in MeCN (2 mL) was added an aqueous solution (12 mL) of potassium hydroxide (56 mg, 1.00 mmol). The reaction was stirred at r.t. for 15 minutes. Then, an aqueous solution of NaAuCl$_4$ (398 mg, 1.00 mmol) (12 mL) was added. The solution was allowed to stir overnight at r.t. in the dark. The brown solid was filtered off, washed with water, ethanol and diethyl ether and dried under vacuum. Yield: 0.419 g (91%). ESI-MS (MeCN, positive mode) exact mass for $C_{12}H_9AuCl_2N_3$ ([M+H]$^+$, theoretical m/z 461.9839): found m/z 461.9832 (err. -1.5 ppm). NMR ^1H (DMSO-d_6, 500 MHz): 9.24 (m, 1H, H^6), 8.46 (m, 1H, H^4), 8.36 (m, 2H, H^3 + H$^{3'}$), 7.86 (m, 1H, H^5), 7.74 (m, 1H, H$^{6'}$), 7.27 (m, 2H, H$^{4'}$ + H$^{5'}$). NMR $^{13}C\{^1H\}$ (DMSO-d_6, 126 MHz): 156.6 (C^{IV}), 149.1 (C^{IV}), 146.1 (CH^6), 144.7 (CH^4), 142.6 (C^{IV}), 140.6 (C^{IV}), 126.4 (CH^5), 124.4 (CH^3), 124.3 (CH$^{4'}$), 122.5 (CH$^{5'}$), 120.2 (CH$^{6'}$), 114.3 (CH$^{3'}$).

Synthesis of [Au(1-methyl-2-[2-pyridyl]-1H-benzo[d]imidazole)Cl$_2$][PF$_6$] – 4: To a solution of 1-methyl-2-[2-pyridyl]-benzimidazole (0.134 g, 0.64 mmol) in MeCN (2.5 mL) was added an aqueous solution of NaAuCl$_4$ (255 mg, 0.64 mmol) (15 mL) and solid KPF$_6$ (0.354 g, 1.92 mmol). The solution was stirred for 3 h at room temperature. The solid was filtered off and washed with water, ethanol and diethyl ether. The light orange solid was recrystallized from acetone-diethyl ether. Yield: 0.327 g (82%). Anal. Calculated for $C_{13}H_{11}AuCl_2F_6N_3P$: C 25.10; H 1.78; N 6.75 %; found: C 25.54; H 1.55; N 6.63 %). ESI-MS (MeCN, positive mode) exact mass for $C_{13}H_{11}AuCl_2F_6N_3P$ ([M-PF$_6$]$^+$, theoretical m/z 475.9996): found m/z 475.9993 (err. -0.6 ppm). NMR ^1H (DMSO-d_6, 500 MHz): 8.93 (m, 1H, H^6), 8.30 (m, 1H, H^3), 8.22 (m, 1H, H^4), 8.02 (m, 1H, H$^{3'}$), 7.87 (m, 1H, H$^{6'}$), 7.81 (m, 1H, H^5), 7.60-7.63 (m, 2H, H$^{4'}$ + H$^{5'}$). NMR $^{13}C\{^1H\}$ (DMSO-d_6, 126 MHz): 150.4 (CH^6), 147.3 (C^{IV}), 143.6 (C^{IV}), 138.4 (CH^4), 134.2 (C^{IV}), 132.0 (C^{IV}), 127.1 (CH^5), 126.5 (CH$^{5'}$), 126.3 (CH^3),

126.2 (CH$^{4'}$), 115.3 (CH$^{6'}$), 113.3 (CH$^{3'}$).
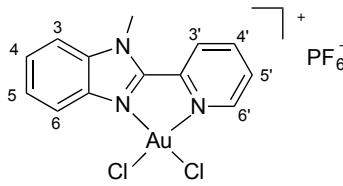
Ethics Statement: Venous blood samples were obtained from healthy human volunteers following a protocol approved by the Ethics Committee of the Faculty of Pharmacy of the University of Lisbon. Informed written consent was obtained from all participants.

Erythrocyte sampling and preparation: Venous blood samples were collected in citrate anticoagulant (2.7 % citric acid, 4.5 % trisodium citrate and 2% glucose). Fresh blood was centrifuged at 750 x*g* for 5 min at 4º C and plasma and buffy coat were discarded. Packed erythrocytes were washed three times in PBS (KCl 2.7 mM, KH2PO4 1.76 mM, Na$_2$HPO$_4$ 10.1 mM, NaCl 137 mM, pH 7.4), diluted to 0.5 % haematocrit and immediately used for experiments. hRBC mean volume in isotonic solution was determined using a CASY-1 Cell Counter (Schärfe System GmbH, Reutlingen, Germany) and was calculated as 82 fL.

Stopped-flow light scattering experiments: Stopped-flow experiments were performed on a HI-TECH Scientific PQ/SF-53 apparatus, with 2 ms dead time, temperature controlled and interfaced with a microcomputer. Experiments were performed at 23 ºC for glycerol permeability (P_{gly}) and at 10 ºC for osmotic water permeability (P_f); for activation energy measurements temperatures were ranged from 10 ºC to 37 ºC. For each experimental condition, 5-7 replicates were analysed. For measuring the osmotic P_f, 100 μL of a suspension of fresh erythrocytes (0.5 %) was mixed with an equal volume of PBS containing 200 mM sucrose as a non-permeable osmolyte to produce a 100 mM inwardly directed sucrose gradient. The kinetics of cell shrinkage was measured from the time course of 90º scattered light intensity at 400 nm until a stable light scatter signal was attained. P_f was estimated by $P_f = k\ (V_o/A)(1/V_w(osm_{out})_\infty)$, where V_w is the molar volume of water, V_o/A is the initial cell volume to area ratio and $(osm_{out})_\infty$ is the final medium osmolarity after the applied osmotic gradient and k is the single exponential time constant fitted to the light scattering signal of erythrocyte shrinkage. For P_{gly}, 100 μL of erythrocyte was mixed with an equal volume of hyperosmotic PBS containing 200 mM glycerol creating a 100 mM inwardly directed glycerol gradient. After the first fast cell shrinkage due to water outflow, glycerol influx in response to its chemical gradient was followed by water influx with subsequent cell reswelling. P_{gly} was calculated as $P_{gly} = k\ (V_o/A)$, where k is the single exponential time

constant fitted to the light scattering signal of glycerol influx in erythrocytes. For inhibition experiments cells were incubated with different concentrations of complexes, from freshly prepared stock aqueous solutions, for various times at r.t. before stopped-flow experiments. A time dependent inhibition assay for all the tested compounds over several hours incubation with hRBC showed no further increase of inhibition after 30 min at r.t. Inhibition reversibility was tested by 30 min incubation of hRBCs with the compounds followed by further incubation with 1 mM 2-mercaptoethanol (EtSH) for 30 min at r.t.. The reversibility assays were also performed under the same conditions, using 1 mM L-cysteine. The inhibitor concentration necessary to achieve 50% inhibition (IC_{50}) was calculated by nonlinear regression of dose-response curves (Graph Pad Prism, Inc) to the equation: $y=y_{min}+(y_{max}-y_{min})/(1+10((LogIC_{50}-Log[Inh]) H))$, where y is the percentage inhibition obtained for each concentration of inhibitor [Inh] and H is the Hill slope. The activation energy (E_a) of water and glycerol permeation was calculated from the slope of the Arrhenius plot (lnP_f or lnP_{gly} as a function of $1/T$) multiplied by the gas constant R. All solution osmolarities were determined from freezing point depression on a semi-micro osmometer (Knauer GmbH, Berlin, Germany) using standards of 100 and 400 mOsM.

Statistical analysis: Data were presented as mean ± standard error of the mean (SEM) of at least four independent experiments, and were analysed with either the paired Student's t-test or one-way analysis of variance (ANOVA) followed by Tukey's test. A value of P = 0.01 was considered to be statistically significant.

Homology modelling and molecular dynamics: The 3D structure of hAQP3 was obtained by homology modelling using the Molecular Operating Environment (MOE 2013.08).[5] The choice of a template structure was based on the sequence identity between hAQP3 and the sequence of the AQPs with available resolved structures. The isoform showing the highest sequence similarity with hAQP3 is the bacterial isoform GlpF, with 34.68% of sequence identity, which was then chosen as a template structure to generate a homology model of hAQP3. The template was selected among the structures with the best resolution (2.70 Å) without any substrate (pdb 1LDI).[6] The tetrameric form was assembled and the structure was prepared and protonated at pH 7, with the Amber12EHT force field, as described in Spinello et al [7], using the Molecular Operating Environment (MOE 2013.08).[5]. 50 intermediate models of AQP3 were generated and averaged to obtain the final homology model. The model obtained was checked for reliable rotamers involving the side chains in the regions of ar/R SF and NPA, by comparison with the available crystal structures of all the other human and microbial AQP isoforms (pdb codes 1H6I, 3GD8, 3D9S, 1RC2, 1LD1 and 3C02). The structure was protonated at pH 7 and an energy minimization refinement was performed, with fixed Cα atoms.

Afterwards, the effect of binding of Au(III) complex **4** on AQP3 glycerol permeability was investigated using classical molecular dynamics (MD). The molecular system consisted of the homology model of the hAQP3 tetramer within a double layer of 166 palmitoyl-oleyl-phosphatidyl-coline (POPC) lipid, prepared using the charmm-gui online server [8,9], using Amber99SB-ILDN in combination with the Slipids (Stockholm lipids) force field for lipids.[10,11] Four glycerol molecules were placed into the system, one above each pore entrance, approximately 30 to 35 Å (to residue TRY212 at the pore entrance). The system was solvated with 35379 water molecules and used a modified amber99sb-ildn force field, with the parameters for glycerol and 1-methyl-2-(pyridine-2-yl)-benzimidazole generated by the Automated Topology Builder and Repository (ATb, version 2.2) website using the B3LYP/6-31G* basis set [12], using a combination of semi-empirical QM and DFT. Complex **4** was parameterised using DFT and QM/MM in order to obtain the parameters for the Au(III) ions in the force field. Afterwards, the complex was bound to the thiolate of a cysteine residue, to further integrate in the protein complex. The complex's geometry was further optimised (Figure S2) and then incorporated into monomer A of AQP3.

All simulations were run using the GROMACS 5.1.2 simulation software.[13] Particle-mesh Ewald method was used for calculating electrostatic interactions. The verlet cut-off scheme with a cut-off distance of 4.0 nm was used for short-range repulsive and attractive interactions and Lincs was used to constrain all bond lengths. Nose-hoover temperature coupling was used to maintain the temperature of the system (τ = 0.5 ps) at 310 K. The Parrinello-Rahman algorithm was used to maintain the pressure of the system at 1 bar with a coupling constant of τ = 1.0 ps. Simulations were equilibrated for 100 ps before production.

The four individual glycerol molecules were defined in the index and coupled in the pull code (e.g. gly_1 to chain_A). A total of 10 MD simulations (5 with the Au(III) complex present and 5 without) were run for 0.5 ns using the direction COM pull procedure, in each case applying a separate yet equal harmonic restraint force to each solute molecule of 600 kJ mol^{-1}nm^2 with a rate of 0.02 nm ns^{-1} along the z-axis.

Two 4000000 step runs or 8 ns were run using the same two model systems and parameters. For these runs the pull code was omitted, therefore removing any biasing of the system.

Pore size measurements: Each pore radius was calculated using the Hole 2.0 program[14], which determines the internal surface based on atomic van der Waals radii. A snapshot at the beginning of each simulation was taken and coordinates for the centre of each pore (monomers A to D), at the ar/R SF, were used to generate

the pore radius along the z-axis.

In order to assess if the gold complex significantly affects the pore size by inducing protein conformational changes, five simulations, with and without gold complex, were performed. From these, 5 snapshots were taken (100, 300, 450, 600 and 800 frames) and the pore size was measured in each. For consistency, the narrowest part of the pore was considered to be the distance between the side chains of Tyr212 and Arg218 and, for each frame, the distance between the closest N atom of the side chain of Arg218 and C of the aromatic ring of Tyr212. The same methodology was used to assess the pore size of monomer A for the long (8 ns) simulation.

DFT calculations: DFT calculations were performed on the structures of cysteine, HCl, Auphen, **2**, **3**, **4** and on the adducts obtained by substituting one chlorido with a cysteinato ligand (see Figure S7), by using the M06-L [15] functional, the Lanl2dz [16] basis set for Au, S and Cl atoms and the 6-31G(d,p) [17,18] basis set for C, N, O and H atoms. Solvent effects were evaluated by full geometry optimization within the implicit water solvent, reproduced by the polarizable continuum model (PCM).[19] Vibration frequency calculations, within the harmonic approximation, were performed to confirm that each optimized geometry corresponded to a minimum in the potential energy surface. Moreover, vibration frequency calculations allowed us to estimate the standard Gibbs free energy values, at 298.15 K, of each energy minimum structure, both *in vacuum* and in solution. All calculations were performed by the Gaussian 09 program package.[20] The energy values of formation of the gold complex-Cys adducts, reported in Table S2, were obtained by the following hypothetical reaction: $[Au(Ligand)Cl_2]^{n+} + HCys \rightarrow [Au(Ligand)ClCys]^{n+} + HCl$, where n is the charge of the metal complex, and calculated by the Eqn. 0 below, where E can be either the self-consistent field (SCF) energy or the standard Gibbs free energy in solution:

$$\Delta E = E[Au(Ligand)ClCys] + E[HCl] - E[Au(Ligand)Cl_2] - E[HCys] \qquad \text{Eq. 0}$$

Electrochemistry: Cyclic voltammograms were recorded using a PalmSens EmStat3+ potentiostat. Compounds (~ 2 mmol) were dissolved in DMSO containing 0.1 M tetrabutylammonium perchlorate (TBAP) as electrolyte and 1 mM ferrocene (Fc) used as internal reference. Measurements were recorded in a single compartment electrochemical cell (0.5 mL volume) containing a glassy carbon disk electrode (3mm diameter), a Ag/AgCl reference electrode and a platinum wire counter electrode. Prior to measurements, the glassy

carbon disc electrode was polished on a microcloth pad in 0.05 μm alumina slurry. All measurements were carried out under nitrogen at r.t..

Initially, we examined the electrochemical response of $HAuCl_4$ in DMSO containing 0.1 M TBAP as a supporting electrolyte. $HAuCl_4$ serves as a useful bench mark to evaluate the effect of the more strongly coordinating N^N and C^N ligands on the redox properties of the Au(III) complexes relative to weakly coordinating chlorido ligands. The electrochemical properties of $HAuCl_4$ have been extensively studied in aqueous [21-25], ionic liquids [26-30] and organic [31-38] electrolytes. In aqueous solution, the reduction of Au(III) to Au(0) takes place in a single three electron reduction process [22,23,25]. However, in aprotic organic media, reduction of Au(III) to Au(0) is postulated to occur in two distinct electrochemical steps [34-37]:

$$AuCl_4^- + 2e^- \rightarrow AuCl_2^- + 2Cl^- \qquad \text{(Eqn. 1)}$$

$$AuCl_2^- + e^- \rightarrow Au + 2Cl^- \qquad \text{(Eqn. 2)}$$
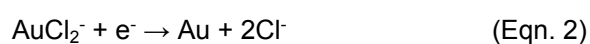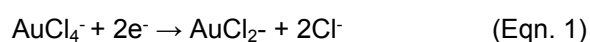
Figure S8 shows the CV of $HAuCl_4$ in DMSO containing 0.1 TBAP as supporting electrolyte. Due to the reactive nature of Au complexes at positive potentials (> +1.23 V vs. Ag/AgCl) [39], the scan was initiated at -0.1 V (indicated by *) to ensure that the Au metal centre was in the +3 oxidation state prior to measurement. Scanning to lower, more negative, potentials generated two successive reduction peaks centred at -0.35 V (peak I) and −1.26 V (peak II) which, in accordance with analogous studies [34-37], can be attributed to Au(III)→Au(I) and Au(I)→Au(0) transitions, respectively.

The absence of defined oxidation peaks on the reverse scan, between -1.9 and 0 V vs. Fc, indicates that both reduction processes are non-reversible. A broad oxidation peak (Peak III) centred at +0.31 V is evident at higher potentials. This oxidative process is consistently observed in aqueous [24], ionic liquids [27-29] and organic media [40] although its origin is unclear and has been attributed to both oxidation of free Cl⁻ ions [36,37] and electrodeposited Au(0) [31,32,40] at the electrode surface. In order to investigate this further, a scan was performed where the switching potential was reversed at -0.9 V, thus preventing subsequent reduction to Au(0) (Figure S8 red scan). No evidence of the corresponding Au oxidation peak was observed indicating that the origin of the oxidation peak is dependent on the formation of Au(0) generated from the Au(I) reduction step. Furthermore, a thin layer of deposited Au(0) was visually observed on the working electrode surface after the two step reduction process. It is likely that this deposited Au(0) undergoes a anodic 'stripping' process at sufficiently positive potentials giving rise to the observed anodic peak [39].

Interestingly, the peak attributed to Au(I) reduction (Peak II') occurs at the same potential for that of $HAuCl_4$ complex. This suggests that the products of both reactions are similar in character. Indeed, this is reasonable

as the postulated mechanism for Au(III) reduction results in liberation the free ligand to form $AuCl_2^-$ (Eqn 3).

Therefore, it is likely that the $1e^-$ reduction of $AuCl_2$ to $Au(0)$ gives rise to the reduction peak.

$$Au(N^\wedge N)Cl_2 + 2e^- \rightarrow AuCl_2^- + N^\wedge N \qquad \text{(Eqn. 3)}$$
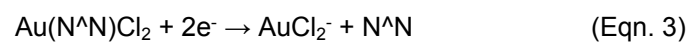
Tables and Figures

Table S1: IC$_{50}$ (µM) values for the gold complexes as human AQP3 inhibitors.

Compound	IC$_{50}$[a]
Auphen	0.8 ± 0.1[b]
1	> 20
2	> 50
3	> 50
4	0.6 ± 0.1

[a] Mean ± SE of at least three independent experiments. [b] from reference [41].
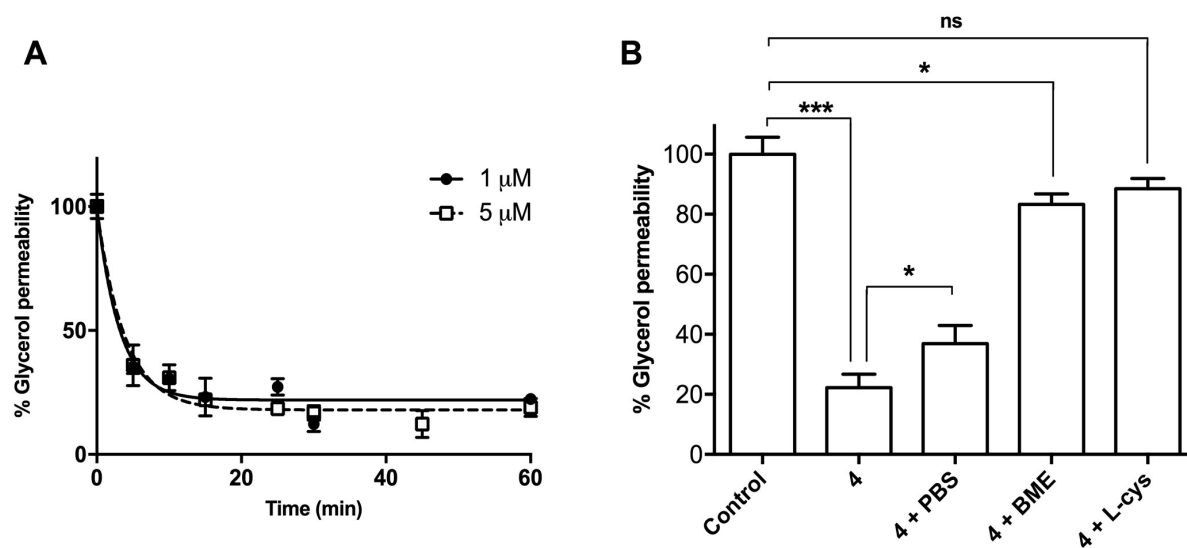
Figure S1 - A: Time-dependence of glycerol permeability (% of control) for two concentrations of **4**; **B**: Inhibition of glycerol permeability (% of control) of hRBCs after treatment with **4** (30 min at r.t., 1 µM), and reversibility by incubation with BME and L-Cys (1 mM for 30 min). The results represent the average of at least three independent experiments ± SE.
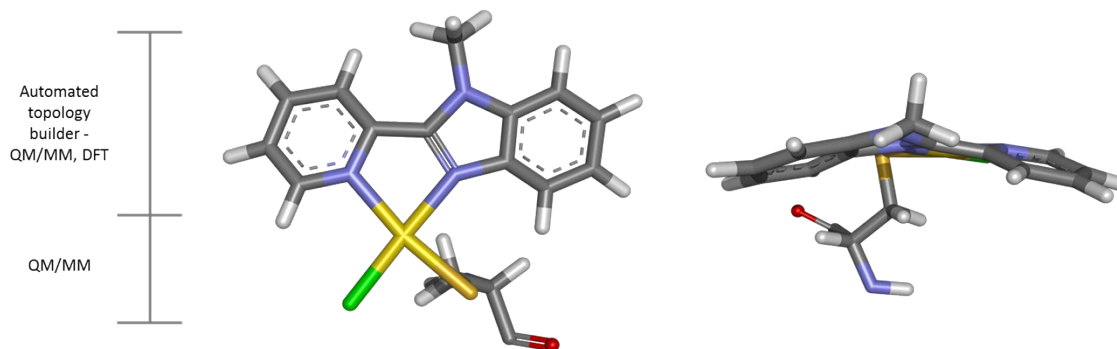
Figure S2. Geometry of modified Cys40 with complex **4** after energy minimisation.
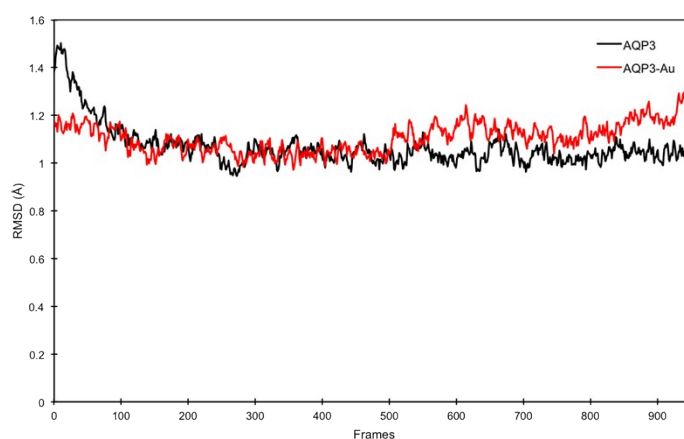
Figure S3. RMSD (Å) of the protein backbone atoms of AQP3 (black) and AQP3-Au (red).
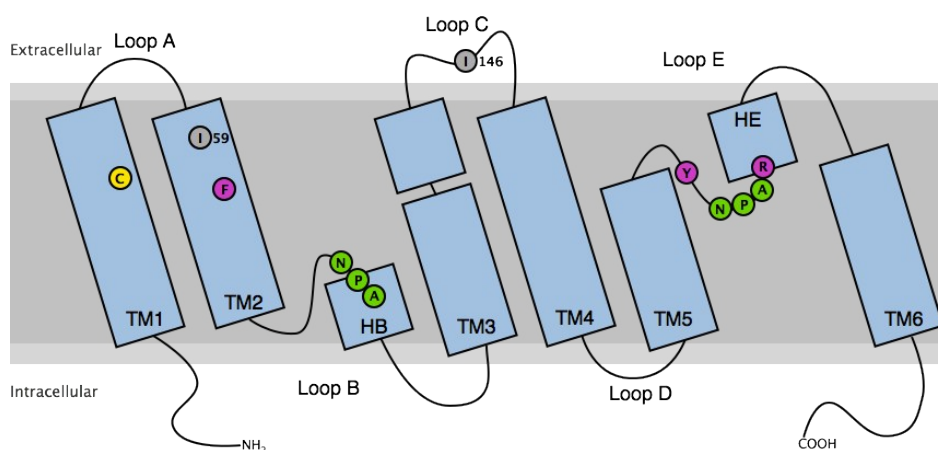

Figure S4 – Schematic representation of the tridimensional structure of AQP3, with helices represented by light blue blocks and loops in black lines. Representative amino acid residues are shown in coloured circles, where ar/R SF residues are shown in magenta and NPA motif in green. Cys40, the Au-binding site is shown in yellow while the two Isoleucines predicted to stabilize the ligand of complex **4** are displayed in grey. Transmembrane helices are numbered TM1-6, while loops are named from A-E. The short-helices that contain the NPA motifs are located in loops and are named according to the respective position, HB or HE.
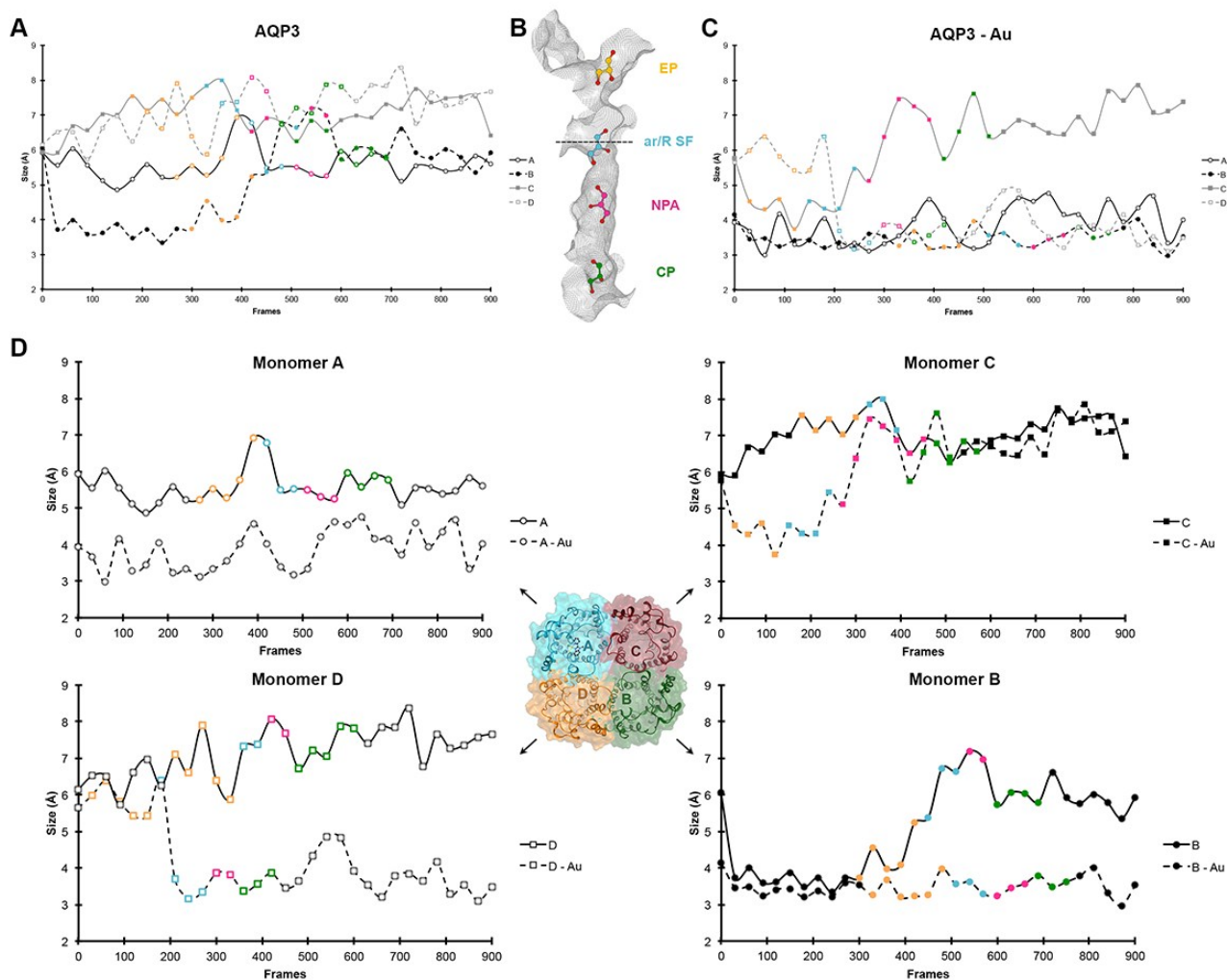
Figure S5 – Pore size taken at the narrowest point of the channel (ar/R SF), from a representative simulation (0.5 ns) of AQP3 permeation by glycerol in the absence **(A)** or presence **(C)** of the gold complex. Each monomer is represented by a trace, and the colored markers indicate the glycerol passage from extracellular to cytoplasmic side. **(B)** Pockets for glycerol passage, indicated in yellow (extracellular pocket), blue (ar/R SF), pink (NPA motif) and green (cytoplasmic pocket). The narrowest point of the channel is indicated by a dashed line (approximate localization). In panel D the pore sizes of each monomer are shown, with (dashed line) and without (full line) gold complex. The same color code of the point markers was used.
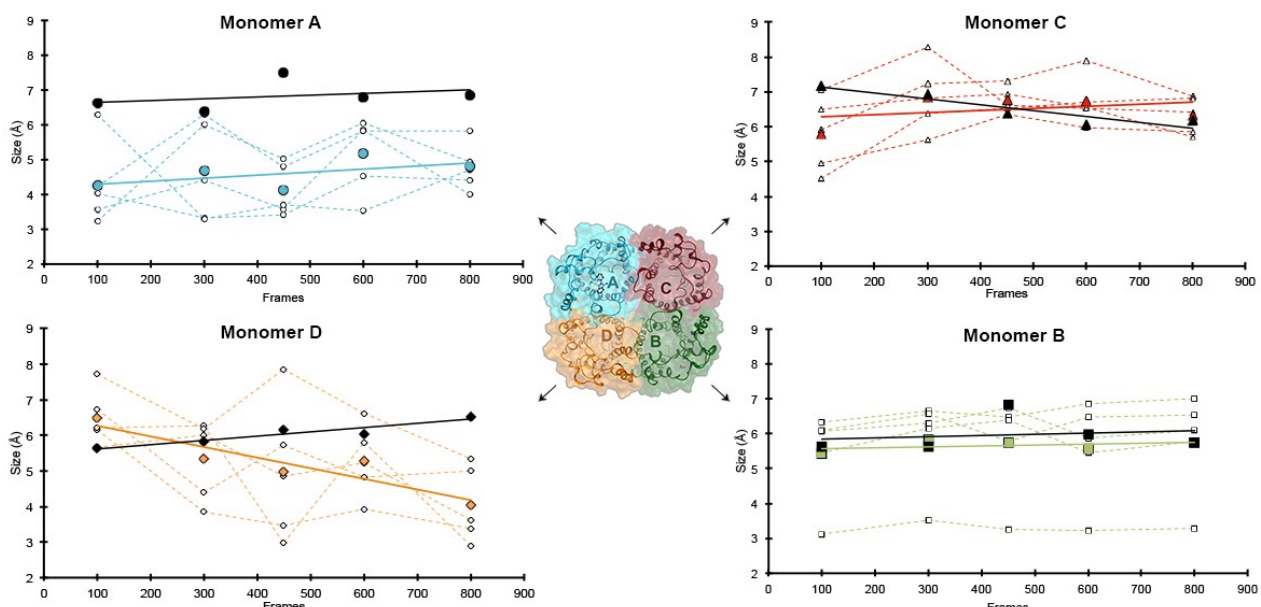
11

Figure S6 – Pore size taken at the narrowest point of the channel (ar/R SF) from 10 independent simulations (0.5 ns) of AQP3 (5 without and 5 with gold complex) for each monomer. In black markers, the pore sizes of each monomer are show as an average of 5 independent simulations and with a linear trend line (shown in black). In colored dashed lines with white markers, the results for each of the 5 individual simulations of AQP3 with the gold complex are shown. In colored markers is represented the average size for each point, for AQP3 with gold complex **4**, with an added linear trend line, shown in the respective color.
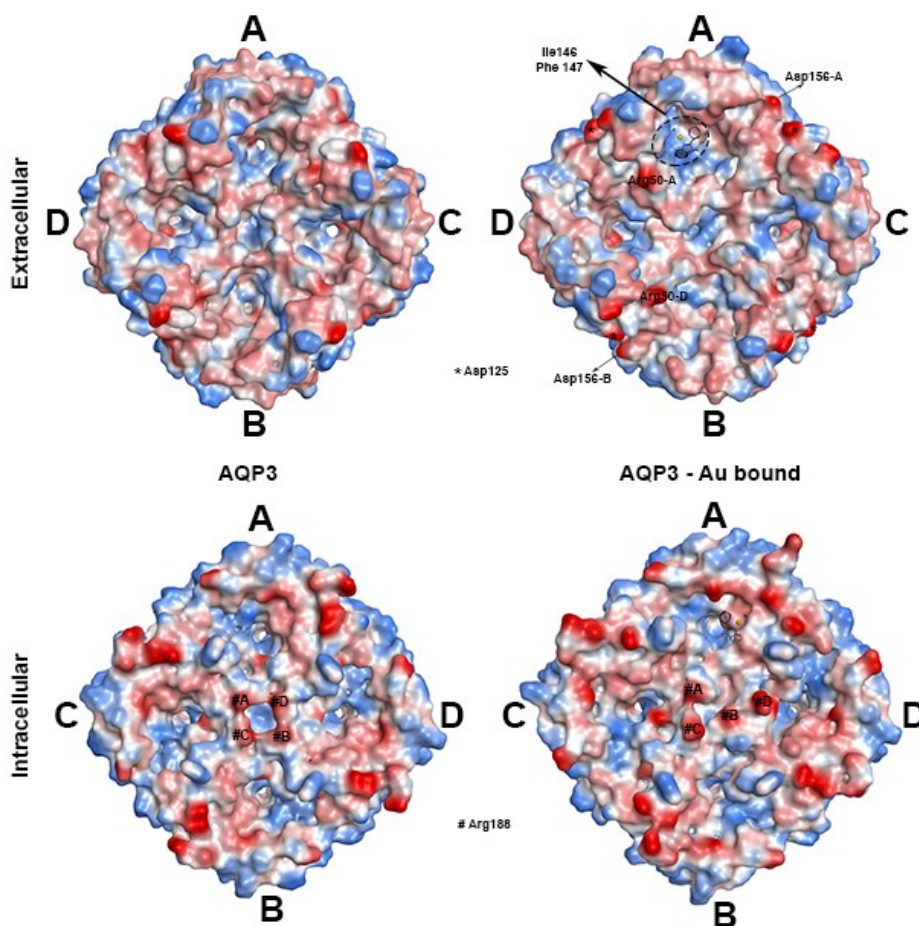

Figure S7 - Top intra and extracellular view of AQP3 (left) and AQP3-Au bound (right) tetramers hydrophobic surfaces at the start of the simulation. Gold complex is shown over the surface only for indication of its relative position within the tetramer. This does not represent the compound's location across the z-axis. Blue = hydrophobic, red = hydrophilic. Generated with MOE.[5]
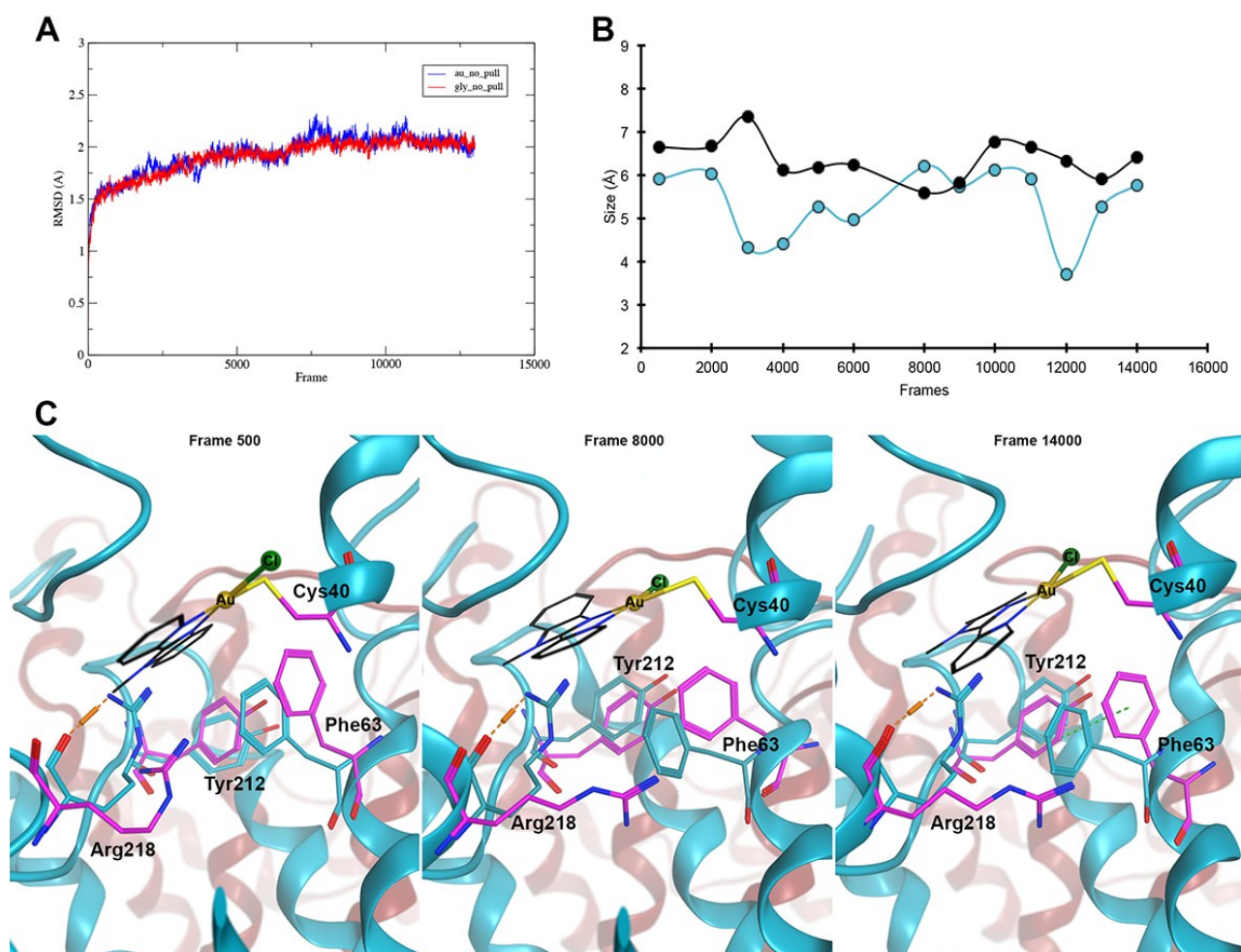
12

Figure S8 – Molecular dynamics simulation of AQP3 permeation by glycerol in the presence and absence of the gold complex without pull (8 ns). During the time of the simulation, due to the absence of pull, any of the glycerol molecules crosses the AQP3 channels. **A)** RMSD of the backbone of AQP3's simulation with (blue trace) and without (red trace) gold complex. **B)** Pore size of monomer A, measured at the narrowest point of the channel. The simulation with gold complex is shown in blue markers and line, while the simulation without the complex is shown in black. **C)** Structure of the ar/R SF of AQP3 (blue) and upon binding of the gold complex (pink). The gold complex **4** is shown in black with thin sticks, gold in yellow-gold color and chloride in green, both in ball and stick representation. H-bonds are shown in orange dashed lines, while H-arene interactions are shown in green dashed lines. The figures in panel C were generated with MOE.[5]
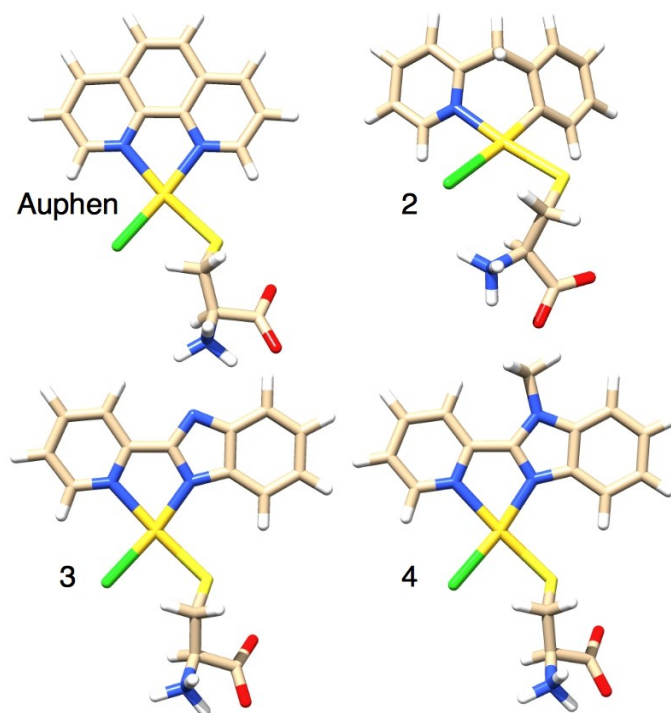
Figure S9. Structure of the cysteinato complexes [Au(ligand)ClCys]$^{n+}$ obtained for Auphen, **2**, **3** and **4**, whose geometry was optimized by DFT calculations; n = 1, 0, 0, 1, for the adducts of Auphen, **2**, **3** and **4**, respectively.

Table S2. Formation energy of [Au(ligand)ClCys]$^{n+}$ adducts in H_2O solution (in kJ/mol, in terms of the SCF energy, ΔE, and of standard Gibbs free energy, ΔG°) calculated through DFT and by Eq. 0.

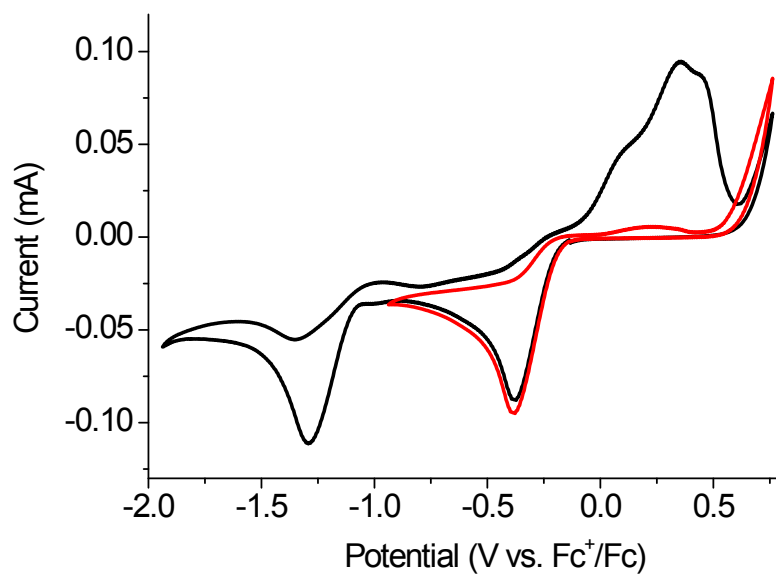| Compound	ΔE	ΔG°
[Au(phen)ClCys]$^+$	-53.7	-45.0
2 [Au(py^b)ClCys]	-10.7	-0.2
3 [Au(PbIm)ClCys]	-27.8	-18.9
4 [Au(PbImMe)ClCys]$^+$	-53.0	-46.6

Figure S10. Cyclic voltammograms of AuCl$_4^-$ in DMSO containing 0.1 M TBAP electrolyte at 0.1 V s^{-1} scan rate. Cathodic sweep initiated at -0.1 V vs. Fc$^+$/Fc. Switching potential -1.95 V vs. Fc$^+$/Fc (black scan) and -0.9 V vs. Fc$^+$/Fc (red scan).
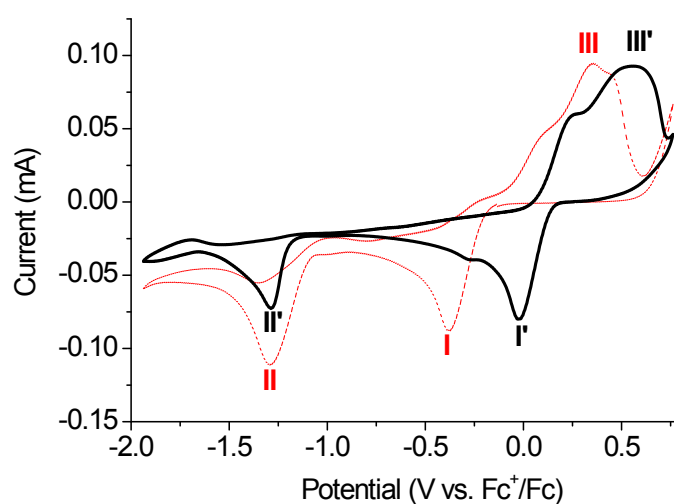

Figure S11. Cyclic voltammograms of Auphen (black) and HAuCl$_4$ (red dash) recorded in DMSO containing 0.1 M TBAP electrolyte at 0.1 V s^{-1} scan rate.

Table S3. List of electrochemical potentials attributed to reductive (E_{red}) and oxidative (E_{ox}) electrochemical processes. Potentials evaluated from cyclic voltammetric scans recorded in DMSO containing 0.1 M TBAP electrolyte at 0.1 V s^{-1} scan rate. All potentials measured against ferrocene/ferrocenium redox couple.

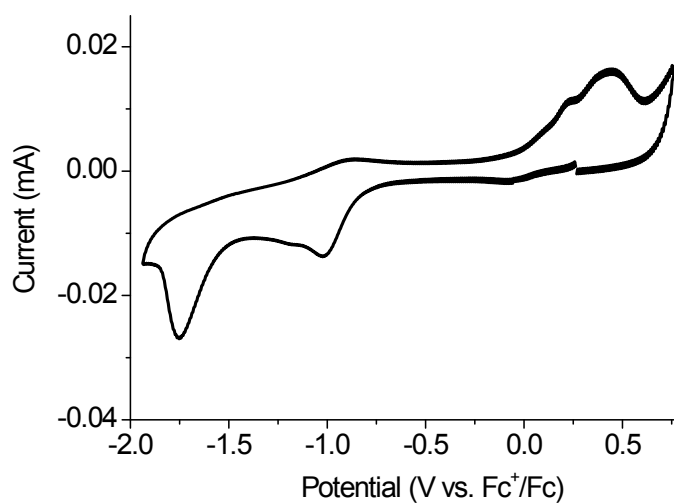| Compound	E_{red} (peak I)	E_{red} (peak II)	E_{ox} (peak III)
HAuCl$_4$	-0.35	-1.26	+0.31
[Au(phen)Cl$_2$]	-0.02	-1.26	+0.49
2 [Au(py^b-H)Cl$_2$]	-0.99	-1.72	+0.38
3 [Au(PbIm)Cl$_2$]	-0.30	-1.16	+0.41
4 [Au(PbImMe)Cl$_2$]PF$_6$	-0.33	-1.28	+0.52

Figure S12. Cyclic voltammogram of complex **2**.
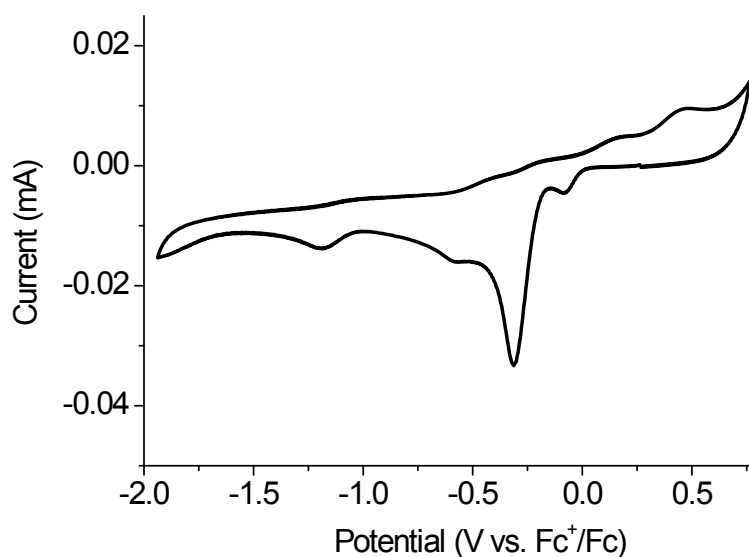

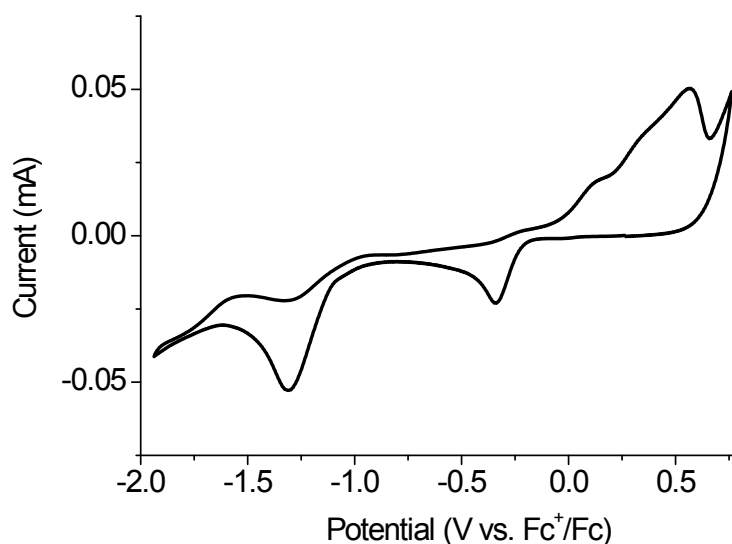**Figure S13.** Cyclic voltammogram of complex **3**.

Figure S14. Cyclic voltammogram of complex **4**.

Videos

AQP3_GLY.mov - MD simulation of human AQP3 glycerol permeation.

AQP3_Au_Complex.mov - MD simulation of glycerol permeation via AQP3 with Au(III) complex **4** bound.

au_gly_2.mov and au_gly_3.mov – Additional MD simulation of glycerol permeation via AQP3 with Au(III)

complex **4** bound.

References

1. Casini A, Diawara MC, Scopelliti R, Zakeeruddin SM, Grätzel M, Dyson PJ. Synthesis, characterisation and biological properties of gold(III) compounds with modified bipyridine and bipyridylamine ligands. *Dalton transactions.* 2010;39:2239-2245.
2. Cinellu MA, Zucca A, Stoccoro S, Minghetti G, Manassero M, Sansoni M. Synthesis and characterization of gold(III) adducts and cyclometallated derivatives with 6-benzyl- and 6-alkyl-2,2[prime or minute]-bipyridines. *Journal of the Chemical Society, Dalton Transactions.* 1996(22):4217-4225.
3. Hollis LS, Lippard SJ. Aqueous chemistry of (2,2',2"-terpyridine)gold(III). Preparation and structures of chloro(2,2',2"-terpyridine)gold dichloride trihydrate ([Au(terpy)Cl]Cl2.3H2O) and the mixed valence gold(I)-gold(III) salt bis[chloro(2,2',2"-terpyridine)gold] tris(dichloroaurate) tetrachloroaurate ([Au(terpy)Cl]2[AuCl2]3[AuCl4]). *Journal of the American Chemical Society.* 1983/06/01 1983;105(13):4293-4299.
4. Bertrand B, Spreckelmeyer S, Bodio E, et al. Exploring the potential of gold(iii) cyclometallated compounds as cytotoxic agents: variations on the C^N theme. *Dalton transactions.* 2015;44(26):11911-11918.
5. Molecular Operating Environment (MOE) CCGI, 1010 Sherbooke St. West, Suite #910, Montreal, QC, Canada, H3A 2R7, 2017.
6. Fu D, Libson A, Miercke LJ, et al. Structure of a glycerol-conducting channel and the basis for its selectivity. *Science.* Oct 20 2000;290(5491):481-486.
7. Spinello A, de Almeida A, Casini A, Barone G. The inhibition of glycerol permeation through aquaglyceroporin-3 induced by mercury(II): A molecular dynamics study. *Journal of inorganic biochemistry.* Jul 2016;160:78-84.

8.   Jo S, Kim T, Iyer VG, Im W. CHARMM-GUI: a web-based graphical user interface for CHARMM. *Journal of computational chemistry.* Aug 2008;29(11):1859-1865.
9.   Wu EL, Cheng X, Jo S, et al. CHARMM-GUI Membrane Builder toward realistic biological membrane simulations. *Journal of computational chemistry.* 2014;35(27):1997-2004.
10.   Jambeck JP, Lyubartsev AP. Another Piece of the Membrane Puzzle: Extending Slipids Further. *Journal of chemical theory and computation.* Jan 08 2013;9(1):774-784.
11.   Jambeck JP, Lyubartsev AP. An Extension and Further Validation of an All-Atomistic Force Field for Biological Membranes. *Journal of chemical theory and computation.* Aug 14 2012;8(8):2938-2948.
12.   Malde AK, Zuo L, Breeze M, et al. An Automated Force Field Topology Builder (ATB) and Repository: Version 1.0. *Journal of chemical theory and computation.* Dec 13 2011;7(12):4026-4037.
13.   Abraham MJ, Murtola T, Schulz R, et al. GROMACS: High performance molecular simulations through multi-level parallelism from laptops to supercomputers. *SoftwareX.* 9// 2015;1–2:19-25.
14.   Smart OS, Neduvelil JG, Wang X, Wallace BA, Sansom MS. HOLE: a program for the analysis of the pore dimensions of ion channel structural models. *Journal of molecular graphics.* Dec 1996;14(6):354-360, 376.
15.   Zhao Y, Truhlar DG. A new local density functional for main-group thermochemistry, transition metal bonding, thermochemical kinetics, and noncovalent interactions. *The Journal of chemical physics.* Nov 21 2006;125(19):194101.
16.   Hay PJ, Wadt WR. Ab initio effective core potentials for molecular calculations. Potentials for the transition metal atoms Sc to Hg. *The Journal of chemical physics.* 1985;82(1):270-283.
17.   Hariharan PC, Pople JA. The influence of polarization functions on molecular orbital hydrogenation energies. *Theoretica chimica acta.* 1973// 1973;28(3):213-222.
18.   Francl MM, Pietro WJ, Hehre WJ, et al. Self-consistent molecular orbital methods. XXIII. A polarization-type basis set for second-row elements. *The Journal of chemical physics.* 1982;77(7):3654-3665.
19.   Tomasi J, Mennucci B, Cammi R. Quantum mechanical continuum solvation models. *Chemical reviews.* Aug 2005;105(8):2999-3093.
20.   *Gaussian 09* [computer program]. Wallingford, CT, USA: Gaussian, Inc.; 2009.
21.   Anderson JE, Sawtelle SM. In situ generation and characterization of gold(I) complexes from K[AuCl4] in aqueous solutions. *Inorganica Chimica Acta.* 1992/04/15 1992;194(2):171-177.
22.   Holt KB, Sabin G, Compton RG, Foord JS, Marken F. Reduction of Tetrachloroaurate(III) at Boron-Doped Diamond Electrodes: Gold Deposition Versus Gold Colloid Formation. *Electroanalysis.* 2002;14(12):797-803.
23.   Boxley CJ, White HS, Lister TE, Pinhero PJ. Electrochemical Deposition and Reoxidation of Au at Highly Oriented Pyrolytic Graphite. Stabilization of Au Nanoparticles on the Upper Plane of Step Edges. *The Journal of Physical Chemistry B.* 2003/01/01 2003;107(2):451-458.
24.   Zhu S, Gorski W, Powell DR, Walmsley JA. Synthesis, structures, and electrochemistry of gold(III) ethylenediamine complexes and interactions with guanosine 5'-monophosphate. *Inorganic chemistry.* Mar 20 2006;45(6):2688-2694.
25.   Komsiyska L, Staikov G. Electrocrystallization of Au nanoparticles on glassy carbon from HClO4 solution containing [AuCl4]−. *Electrochimica Acta.* 12/30/ 2008;54(2):168-172.
26.   Xu XH, Hussey CL. The Electrochemistry of Gold at Glassy Carbon in the Basic Aluminum Chloride-1-Methyl-3-ethylimidazolium Chloride Molten Salt. *Journal of The Electrochemical Society.* 1992;139(11):3103-3108.
27.   Aldous L, Silvester DS, Villagran C, et al. Electrochemical studies of gold and chloride in ionic liquids. *New Journal of Chemistry.* 2006;30(11):1576-1583.
28.   Oyama T, Yamaguchi S, Rahman MR, Okajima T, Ohsaka T, Oyama N. EQCM study of the [Au(III)Cl4](-)-[Au(I)Cl2](-)-Au(0) redox system in 1-ethyl-3-methylimidazolium tetrafluoroborate room-temperature ionic liquid. *Langmuir : the ACS journal of surfaces and colloids.* Jun 1 2010;26(11):9069-9075.
29.   Oyama T, Okajima T, Ohsaka T. Electrodeposition of Gold at Glassy Carbon Electrodes in Room-Temperature Ionic Liquids. *Journal of The Electrochemical Society.* 2007;154(6):D322-D327.
30.   Papaiconomou N, Glandut N, Billard I, Chainet E. Unusual electrochemical behaviour of AuBr4- in ionic liquids. Towards a simple recovery of gold(iii) after extraction into an ionic liquid. *RSC Advances.* 2014;4(103):58910-58915.
31.   Koelle U, Laguna A. Electrochemistry of Au-complexes. *Inorganica Chimica Acta.* 6/30/ 1999;290(1):44-50.
32.   Messori L, Abbate F, Marcon G, et al. Gold(III) complexes as potential antitumor agents: solution chemistry and cytotoxic properties of some selected gold(III) compounds. *Journal of medicinal chemistry.* Sep 21 2000;43(19):3541-3548.

33. Kouroulis KN, Hadjikakou SK, Kourkoumelis N, et al. Synthesis, structural characterization and in vitro cytotoxicity of new Au(III) and Au(I) complexes with thioamides. *Dalton transactions.* Dec 21 2009(47):10446-10456.

34. Corma A, Domínguez I, Doménech A, et al. Enantioselective epoxidation of olefins with molecular oxygen catalyzed by gold(III): A dual pathway for oxygen transfer. *Journal of Catalysis.* 7/25/ 2009;265(2):238-244.

35. Ballarin B, Busetto L, Cristina Cassani M, Femoni C. A new gold(III)-aminoethyl imidazolium aurate salt: Synthesis, characterization and reactivity. *Inorganica Chimica Acta.* 6/20/ 2010;363(10):2055-2064.

36. Li J, Hu J, Gu Y, Mei F, Li T, Li G. Catalytic activities and properties of Au(III)/Schiff-base complexes in methanol oxidative carbonylation. *Journal of Molecular Catalysis A: Chemical.* 4/23/ 2011;340(1–2):53-59.

37. Monzon LMA, Byrne F, Coey JMD. Gold electrodeposition in organic media. *Journal of Electroanalytical Chemistry.* 7/1/ 2011;657(1–2):54-60.

38. Ongaro M, Gambirasi A, Favaro M, Kuhn A, Ugo P. Asymmetrical modification of carbon microfibers by bipolar electrochemistry in acetonitrile. *Electrochimica Acta.* 1/10/ 2014;116:421-428.

39. Yu L, Andriola A. Quantitative gold nanoparticle analysis methods: A review. *Talanta.* Aug 15 2010;82(3):869-875.

40. Zhang J, Yan P, Li G, Hou G, Suda M, Einaga Y. Systematic investigation of an array of TCNQ lanthanide complexes: synthesis, structure and magnetic properties. *Dalton transactions.* Dec 21 2009(47):10466-10473.

41. Martins AP, Marrone A, Ciancetta A, et al. Targeting aquaporin function: potent inhibition of aquaglyceroporin-3 by a gold-based compound. *PloS one.* 2012;7(5):e37435.